Computers & Geosciences 167 (2022) 105198

Contents lists available at ScienceDirect

Computers and Geosciences

journal homepage: www.elsevier.com/locate/cageo

Research paper

QDM*lab*: A MATLAB toolbox for analyzing quantum diamond microscope (QDM) magnetic field maps

Michael W.R. Volk [a,*], Roger R. Fu [a], Raisa Trubko [a,b,c], Pauli Kehayias [a,d], David R. Glenn [a,c], Eduardo A. Lima [e]

[a] Department for Earth and Planetary Sciences, Harvard University, 20 Oxford Street, Cambridge, MA, 02138, USA
[b] Department of Physics, Worcester Polytechnic Institute, 100 Institute Road, Worcester, MA, 01609, USA
[c] Sandia National Laboratories, Albuquerque, NM, 87123, USA
[d] Department of Physics, Harvard University, 17 Oxford Street, Cambridge, MA, 02138, USA
[e] Department of Earth, Atmospheric, and Planetary Sciences, Massachusetts Institute of Technology, 77 Massachusetts Avenue - Bldg 54, Cambridge, MA, 02139, USA

ARTICLE INFO

Keywords:
Magnetic microscopy
Quantum diamond microscope
MATLAB toolbox
Rock magnetism

ABSTRACT

Paleomagnetic measurements of rock magnetizations are typically performed using classical net moment rock magnetometers on bulk, millimeter- to centimeter-sized samples. In this case, the limited spatial resolution effectively averages across the signal of multiple populations of magnetic grains, each of which may have a distinct geological history. Magnetic field imaging with the quantum diamond microscope (QDM) allows for the measurement of weakly magnetic (10^{-16} Am^2) samples at micrometer spatial resolution, potentially isolating the signal of magnetic grain populations and resolving ambiguities from bulk sample analyses. To achieve such high resolution, the QDM retrieves the energy spectrum of nitrogen–vacancy (NV) color centers within micrometer-scale pixels across a millimeter-scale field of view. Therefore, large amounts of data need to be processed to generate a magnetic field map, which itself often requires further specialized analysis. Until now, no freely-available, comprehensive, open-source software package existed that was able to process this type of data. Here we give an overview of the most important features of QDM*lab*, our open-source MATLAB toolbox for generating and analyzing QDM magnetic field maps of geologic samples. QDM*lab* utilizes modern computational techniques like graphics processing unit (GPU) and spectral fitting routines as well as automated image alignment algorithms. QDM*lab* contains easy-to-use functions for (1) generating magnetic field maps from raw QDM data, (2) map editing, and (3) quantifying the net magnetic moment and rock magnetic properties of rock and mineral samples.

1. Introduction

The study of past magnetic fields of the Earth and other planetary bodies relies on the accurate measurement of a sample's magnetization and understanding the age of magnetization acquisition. Most rocks contain particles or inclusions of ferro- and/or ferri-magnetic minerals, which may have acquired a thermal, chemical, viscous, detrital, or pressure remanent magnetization (Chang et al., 2020; Yu and Tauxe, 2006; Dunlop and West, 1969; McClelland, 1996; Volk and Feinberg, 2019). Chemical changes, reheating events, shock, grain growth, and post-depositional rotation can affect alter or completely reset the magnetic information. These changes are not necessarily homogeneous throughout the whole rock and can vary at micrometer scales. As a result, geological samples may comprise a complex set of disparate magnetic grains. Extracting useful paleomagnetic information from such samples requires understanding the magnetic carriers at sub-millimeter scales.

For decades, paleomagnetists have measured the total natural remanent magnetization (NRM) of bulk rock samples using traditional instruments, such as superconducting quantum interference device (SQUID) based rock magnetometers. These instruments often require large, centimeter-sized rock samples, thereby limiting the spatial resolution of the analysis and integrating over a large number of magnetic particles that may have very distinct magnetic histories and properties. Developments of scanning-SQUID microscopes and, more recently, the quantum diamond microscope (QDM) have enabled the mapping and isolation of magnetic signals at much smaller scales (Weiss et al., 2007; Glenn et al., 2017; Fu et al., 2020).

* Corresponding author.
E-mail address: michael_volk@fas.harvard.edu (M.W.R. Volk).

https://doi.org/10.1016/j.cageo.2022.105198
Received 23 September 2021; Received in revised form 12 July 2022; Accepted 18 July 2022
Available online 23 July 2022

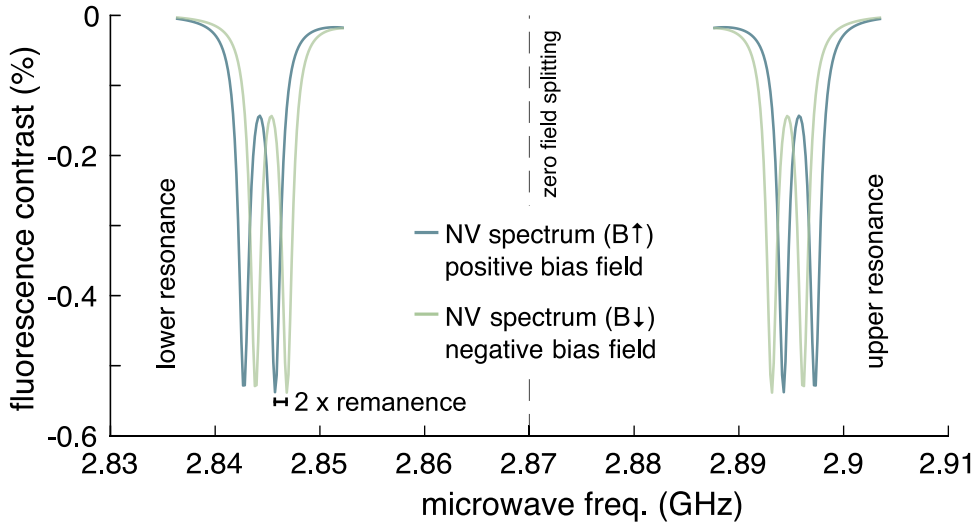

Fig. 1. Sketch of a typical ODMR spectrum of the QDM in PMM mode using a ^{15}N diamond. B↑ and B↓ are, respectively, resonances detected in two magnetic field maps created under a positive and negative bias field (green, blue lines) in the [111] crystallographic direction. For a pixel containing zero signal from remanent magnetization, the resonances detected under the two bias fields, drawn in green and blue, are identical. The existence of a non-reversing field component created by remanent magnetization asymmetrically shifts the separation between the upper and lower resonances, leading to an offset between the spectra taken under the two bias field polarities. Analysis of this shift using QDM*lab* computes the local remanence-generated magnetic field at the location of each pixel. (For interpretation of the references to color in this figure legend, the reader is referred to the web version of this article.)

The QDM's superior resolution, high magnetic moment sensitivity ($\approx 10^{-16}$ Am^2), and ease of use make it a powerful instrument for studying the spatial distribution of magnetic particles and their remanence properties, providing information otherwise inaccessible to bulk-sample magnetometers (e.g. Fu et al., 2021a; Hsieh et al., 2019; Glenn et al., 2015). In addition to the rapid adoption within the paleo- and rock magnetic community, QDM magnetic field maps have applications in other scientific disciplines (e.g. material science, biology). As such, the software presented here, which was designed primarily for geoscience applications, is suitable to any application that uses magnetic field maps generated by the QDM and potentially by other high-resolution imaging magnetometers.

1.1. QDM instrumentation overview

We describe here the basic procedure behind a typical QDM data acquisition sequence to motivate the types of data analysis routines described later in this work.

The QDM measures changes in the optically-detected magnetic resonance (ODMR) spectra to monitor changes in the fluorescence intensity of nitrogen–vacancy (NV) centers in diamond used as a magnetic sensor during a microwave frequency sweep (Fig. 1). To generate the ODMR spectrum, an image is taken by an optical detector (e.g. complementary metal–oxide–semiconductor (CMOS) camera) at each microwave frequency.

Magnetic fields in the vicinity of the NV shift the resonance frequencies, seen as dips in the ODMR spectrum, proportionally to the field strength. In the case of paleomagnetic samples, these static magnetic fields stem from ferro-, ferri-, and paramagnetic grains in the rock sample, which usually has a polished surface placed within a small distance between 1 and 100 μm of the diamond NV centers.

Each NV color center – as defined by the nitrogen atom and corresponding vacancy – in diamond is aligned along one of the four [111] diamond crystal axes and shows a microwave resonance triplet or doublet depending on the use of ^{14}N or ^{15}N NVs, respectively. Analyzing this complex combination of peaks may not be possible if resonances corresponding to different crystal axes overlap. A small DC bias magnetic field (900 - 1400 μT) can be applied along one of the NV axes (projective magnetic microscopy) (Glenn et al., 2017). This field increases the frequency splitting of this NV orientation and separates the chosen NV direction's resonance from that of the other NV axes (Glenn et al., 2017; Fischer et al., 2013). A measurement can be split into two separate microwave frequency sweeps (Fig. 1), one at low and one at high frequency, saving measurement time. For more information on measurement protocols and the physics behind NV-magnetometry and the operating and measurement procedures of the QDM, the reader is directed towards Glenn et al. (2017) and Levine et al. (2019).

The magnetization of a sample measured in a magnetic field is the sum of induced and remanent parts. QDM measurements are conducted in a bias magnetic field, thus each ODMR spectrum also reflects the induced component of magnetization. Paleomagnetists, in most cases, are interested in the remanent part of the magnetization, while the induced magnetization may contain complementary rock magnetic information. For this reason, two separate measurements, with positive (B↑) and negative (B↓) magnetic bias field, are conducted and saved as individual files. Because the induced components are equal and opposite in the B↑ and B↓ maps (Section 5.3.2), the average of the two maps gives the magnetic field due to remanent magnetization alone. The difference between the two, on the other hand, removes the remanent component and isolates the magnetic field signal due to induced magnetization. It is worth noting, that the remanence of particles with coercivities smaller than the bias field (i.e. B_c < 0.9-1.4 mT) may be affected due to irreversible changes in domain wall configuration (Dunlop and Özdemir, 1997).

A typical QDM measurement can consist of several million ODMR spectra, each of which needs to be analyzed to quantify the resonant microwave frequencies at each pixel. Given the sheer amount of data, it becomes clear that fitting spectra manually is unfeasible. A free, easy-to-use, and open-source package is needed to reproducibly calculate magnetic maps from the raw ODMR spectra and to edit and analyze the resulting magnetic maps.

2. Scope of QDM*lab*

QDM*lab* is a MATLAB toolbox tailored towards generating and analyzing QDM magnetic field maps. The functions contained in QDM*lab* can be roughly divided into three categories: (1) magnetic field map generation, (2) map editing, and (3) map analysis (Fig. 2). Early versions of some of individual functions (e.g. `QDMdataprocessing`,

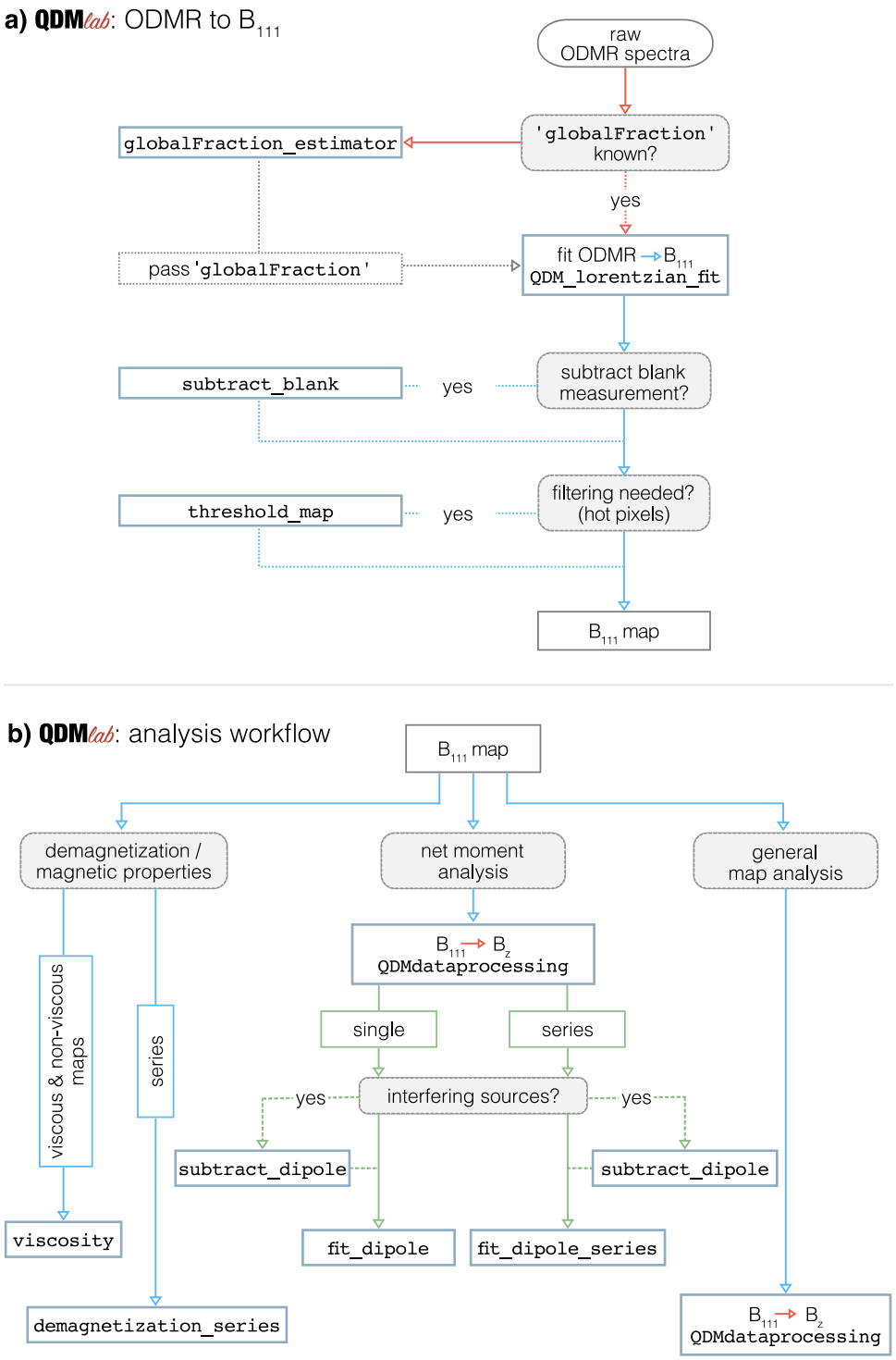

Fig. 2. (a) Workflow from raw ODMR spectra to fitted B_{111} magnetic field map. (b) analysis workflow diagram. `*_series` functions require a set of measurements (i.e. AF/thermal demagnetization). Dashed lines show optional steps.

`demag_analysis`) have been published previously (Fu et al., 2021a, 2020, 2021b; Volk et al., 2021). Most functions, however, like the ODMR spectrum fitting (`ODMR_to_B111`), editing (e.g. `subtract_blank`, `subtract_source`) and analysis (`viscosity`) tools are published here for the first time. This paper provides an in-depth look at the functions contained in QDM*lab* with data, analysis, and code examples. Syntax highlighting will be used throughout the manuscript to distinguish general `functions` or `code`, `keywords`, ⟨*placeholders*⟩ for inputs, *values*, and their *defaults*∗.

2.1. Requirements

The toolbox container (`.mltbx`), which is the preferred method of installation, as well as the source code can be downloaded at https://github.com/HarvardPaleomag/QDMlab/releases. Mathworks MATLAB 2019b or later, and the Mathworks Signal Processing, Computer Vision, and Optimization toolboxes are required for full functionality of QDM*lab*. Additionally, GPUfit (Przybylski et al., 2017) – an open-source CUDA fitting package – is needed for the calculation of magnetic maps from raw ODMR spectra. A pre-compiled version of GPUfit, with all

Table 1
Necessary fields in the ODMR raw data format (`run_*.mat`). All data are of type `double`. n is the total number of pixels (`imgNumRows` × `imgNumCols`).

Variable	Dimensions	Description
`numFreqs`	(1,1)	The number of measured frequencies
`freqList`	(1, 2×`numFreqs`)	A list of all measured microwave frequencies
`imgNumCols`	(1,1)	x number of pixels of the images
`imgNumRows`	(1,1)	y number of pixels of the images
`imgStack1`	(`numFreqs`, n)	All low-frequency spectra (consecutive rows)
`imgStack2`	(`numFreqs`, n)	All high-frequency spectra (consecutive rows)

models needed to fit the ODMR spectra of ^{14}N and ^{15}N diamonds, is included in the toolbox. To test the scripts and function presented here, we provide an tutorial and an extensive collection of raw and processed data for download at https://doi.org/10.7910/DVN/MPMNZI (Volk et al., 2022). Furthermore, a short walk-through tutorial and a small dataset (reduced resolution) can be found in the supplement and at https://github.com/MikeVolk/QDMlab_tutorials

2.2. ODMR raw data format

To convert ODMR spectra into magnetic field maps as described in Section 3, the raw data needs to be formatted correctly. Typically, two data files, one each for B↑ and B↓ (`run_00000.mat`, `run_00001.mat`), a reflected-light image, and an optical map of laser fluorescence are required. The `run_*` MATLAB-7 formatted data files consist of 6 variables (Table 1). `QDMreshape_reverse` helps convert the data into the `imgStack1` and `imgStack2` variables. For example, a (1920, 1200, 50) dataset is converted into (50, 2304000) by layering all columns sequentially. QDMs using measurement software developed by the Harvard Paleomagnetics Lab or by QDM.io LLC will automatically generate the correct file and variable structure.

3. From ODMR spectra to B_{111} data

QDM-generated raw ODMR spectra for each pixel must be first fitted to create a map of magnetic field values. These calculations are done with `ODMR_to_B111`, which uses graphical processor unit (GPU) accelerated curve fitting routines (Przybylski et al., 2017) to convert the raw ODMR spectra from the B↑ and B↓ polarity measurements into remanent and induced parts of the B_{111} magnetic field map (Glenn et al., 2017). First, the data needs to be corrected for the presence of global fluorescence (GF) (Fu et al., 2020). Each pixel's ODMR spectrum is a superposition of fluorescence signals originating from the pixel location and a GF, which consists of internally reflected fluorescence from elsewhere in the diamond. Determining the correct sample-specific value of the GF fraction, defined as the fraction of non-local fluorescence out of the total fluorescence (`globalFraction`, ⟨*0-1*⟩), is an important and non-trivial step in the QDM map analysis. QDM*lab* implements the GF correction as described in Fu et al. (2020) (`correct_global`) and automatically applies it during the fitting process (`globalFraction`). Typical values for the GF fraction range from 0.2 - 0.5.

QDM*lab* includes a simple graphical user interface (GUI) program (Fig. 3) to help determine the optimal GF value. The `globalFraction_estimator` shows the ODMR spectra for 3 pixels. The center panel shows the data of a random pixel after binning and can be changed with the slider on the top of the window. The left and right plots show pixels with the left- and right-most minima. Compared to typical pixels, the larger frequency shifts of these pixels minimize the overlap of the global and local signal. Thus, the GF can be distinguished from the sample signal more easily. The three minima of the global signal are clearly visible in the left and right panels of Fig. 3, while they are hidden in the center spectrum. Using the bottom slider, *globalFraction* is changed until the additional dips (see arrows Fig. 3) in the spectra disappear. An excessive `globalFraction` creates unphysical "peaks" at the edges of the spectra (see left panel of Fig. 3).

The `globalFraction` value, a number between 0 and 1, can be passed to `ODMR_to_B111`.

Apart from the `globalFraction`, `ODMR_to_B111` has keywords that change the behavior and can improve the ODMR fits (Code 1).

```
ODMR_to_B111('nFolders', ⟨{paths}⟩ ...,
  'binSize', ⟨int, 4*⟩ ...,
  'type', ⟨0,1,2*⟩ ...,
  'globalFraction', ⟨double, 0.25*⟩ ...,
  'diamond', ⟨'N14'*, 'N15'⟩ ...)
```

Code 1: Typical usage of `QDMR_to_B111` with essential `keywords` and ⟨*values*⟩. ⟨*{}*⟩ denote MATLAB cells can be passed and ⟨***⟩ default values for the input.

Binning (`binSize`) averages several pixels and resizes the original ODMR spectra array. This effectively reduces noise but lowers the spatial resolution of the image.

`ODMR_to_B111` has 3 options (`type`) to determine the initial guess for the fitting routine (i.e. starting parameters). The simplest option (`type`=0) determines a single initial guess (i.e., dip locations and width, and contrast) from the maps' mean signal, which works well for weak samples. The computationally intensive option `type`=1 estimates an initial guess for each pixel individually (MATLAB function `findpeaks`) and yields better results for strong fields. The default method (`type`=2*) calculates an initial guess by first fitting a single gaussian distribution to the ODMR data, in order to find the center. For data with severely non-uniform baselines, where the baseline intensity shows a linear or otherwise non-flat slope, this method can lead to inconsistent fits in a small number of pixels. This method is fast (GPUfit) and generally more robust than the other methods in the majority of use cases, and all maps presented here were calculated with it.

Passing `checkPlot`=`true` to `ODMR_to_B111` creates plots for each frequency range and field direction (Fig. 4) to verify the quality of the fits. The leftmost plot (Fig. 4a) shows a map of the fitted resonances and the center plot (Fig. 4b) the corresponding misfits (χ^2). Selecting a pixel in either of these plots will plot the data, initial guess (and pre-guess), and fit for that pixel (Fig. 4c). It is recommended to check the quality of the fits by selecting high χ^2 pixels and adjusting the `ODMR_to_B111` parameters if inconsistencies arise. In the case of a failed fit an entry is added to `pixel_alerts` in the `final_fits*.mat` file. Running `ODMR_to_B111` creates the data files `B111dataToPlot.mat` and `final_fits_NxN.mat` where N denotes binning and several diagnostic plots.

3.1. Editing maps

After successfully calculating the B_{111} map, the generated maps may need to be edited to isolate the desired signals. Most functions described in this section are not exclusive to B_{111} data and can be used on B_z maps as well.

3.1.1. B_{111} blank subtraction

Even blank maps show artifacts, which stem from imperfections in the diamond and increase the noise of the overall measurement (e.g. Kehayias et al., 2019) (Fig. 5a,b). Subtracting this background signal of the diamond from the sample data can increase the signal-to-noise ratio

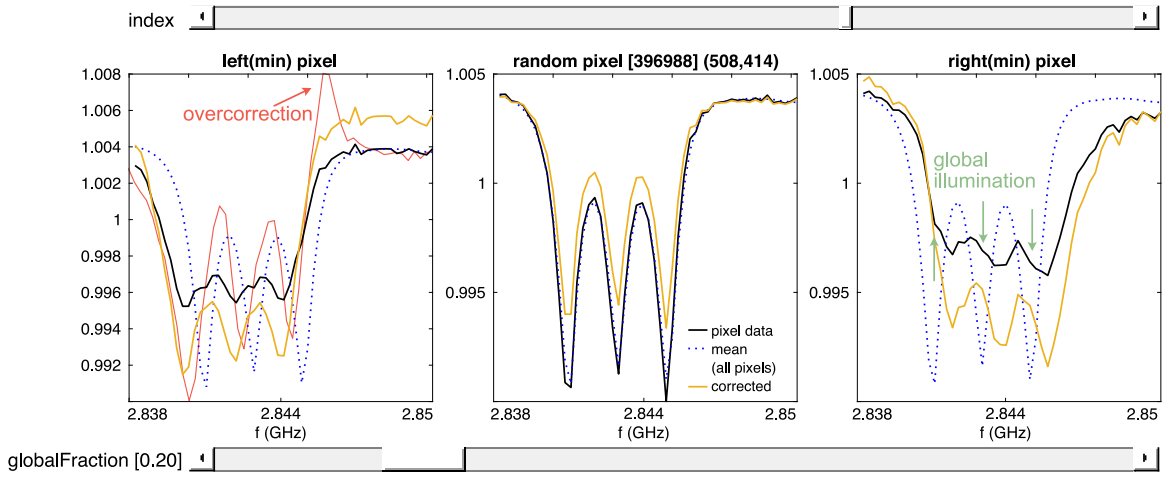

Fig. 3. `globalFraction_estimator` GUI for estimation of the global illumination fraction (`globalFraction`) of a sample (Fu et al., 2020). left panel: pixel with minimum at the lowest frequency. Red line showing overcorrected data (`globalFraction=0.72`) was added for illustration. center panel: a random pixel. Index can be selected with top slider. right panel: pixel with minimum at the highest frequency. Moving the bottom slider changes the `globalFraction` value.

significantly. For successful subtraction of the diamond background signal, it is crucial for pixels corresponding to the same source region in the data and blank maps to be co-located to within a few µm. To correct for small shifts in diamond position, the sample and blank data have to be aligned before subtraction (Fig. 5c).

`subtract_blank` (Code 2) automates the map alignment and blank subtraction. First, `subtract_blank` calculates a 2-D affine geometric transformation of the blank map with respect to the sample using a map of fluorescence intensity, which shows mostly diamond surface features (Fig. 5c). The transformation is calculated by detecting pairs of common features, and their relative translation and rotation (Fig. 5d, e). In most cases, alignment results in a transformation accuracy of 1 or 2 pixels at 4 × 4 binning (Fig. 5e). Finally the magnetic data of the blank map is transformed and subtracted from the sample data (Fig. 5d, e). As an example of the reduction in noise, we use `subtract_blank` on two separately measured blank maps with a small diamond misalignment Fig. 5. Subtraction reduces the RMS noise floor of the original "sample" data from 58 nT to 39 nT and removes most of the scratch-like features visible in Fig. 5a,b). In contrast, a simple subtraction of the two maps without alignment increases the RMS to 75 nT.

```
subtract_blank('nFiles', ⟨{paths}⟩, ...
  'blankFile', ⟨path⟩, ...
  'checkPlot', ⟨bool⟩, ...
  'save', ⟨bool⟩ ...)
```

Code 2: Example for subtracting a blank (`blankFile`) map from multiple measurement files (`nFolders`) using `subtract_blank`.

3.1.2. Threshold map

QDM*lab* contains additional functions for editing maps. Large shifts in resonance can cause fits in `ODMR_to_B111` to diverge and result in unphysical, high field values for individual pixels (hot pixels). Because a spectral algorithm is used to re-project B_{111} data to the vertical field B_z (Lima and Weiss, 2016), these hot pixels (Fig. 6a) become delocalized in the B_z maps and therefore cause major artifacts that appear as vertical 'dotted' lines in the map (Fig. 6b). Hot pixels issues are not limited to $B_{111} \rightarrow B_z$; other analysis branches, such as `demag_behavior` (Section 5.3.1) can also be affected. Therefore, the data should be thresholded to remove misfit-induced extreme outliers before further analysis.

`threshold_map` offers a variety of options to remove hot pixels and save the cleaned data. If called without arguments, `threshold_map` removes all pixels with magnetic field values outside of a conservative > ±500 µT window but can be set to a different value with `threshold`. The removed pixels are replaced by an average of the surrounding pixels (`win`) or `nan` (`win=nan`). Furthermore, `threshold_map` can be used to filter outliers according to the magnetic data or the χ^2 (`chi`) values, where values outside of n standard deviations (defined by `cutOff`) over/below the median get replaced.

4. B_z conversion

After successfully calculating the B_{111} data from the raw ODMR spectra, it is generally more intuitive to work with maps showing the vertical component of magnetic field (B_z). The z-component (x,y also) of the field can be recovered from the B_{111} data with the help of spectral methods (Lima and Weiss, 2016). `QDMdataprocessing` automates the conversion process of B_{111} data into a B_z map of remanent or induced signal (Fu et al., 2020). A variety of map editing features (e.g. `crop_map`, `subtract_constant`) are incorporated into `QDMdataprocessing` and can be applied before the $B_{111} \rightarrow B_z$ conversion. `QDMdataprocessing` requires the user to input the pixel

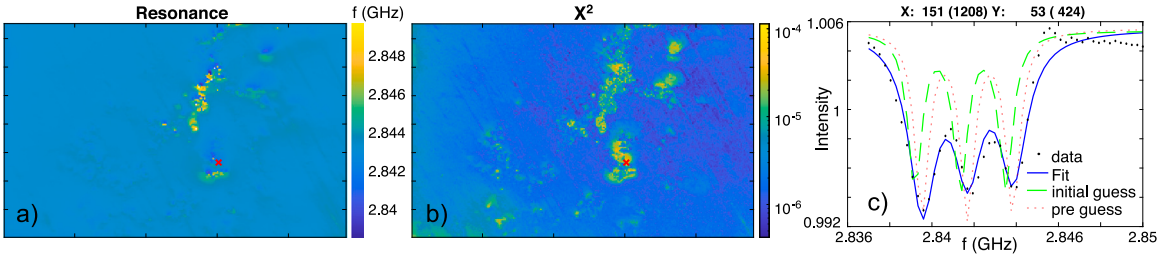

Fig. 4. Plot generated by `ODMR_to_B111` (`'checkPlot', true`) for the low microwave frequency resonance at negative fields. (a) shows the resonance frequency after fitting the data. (b) χ^2 values of the fits. (c) Binned raw data, pre-guess, initial guess and fit of the selected pixel (red cross in a&b).

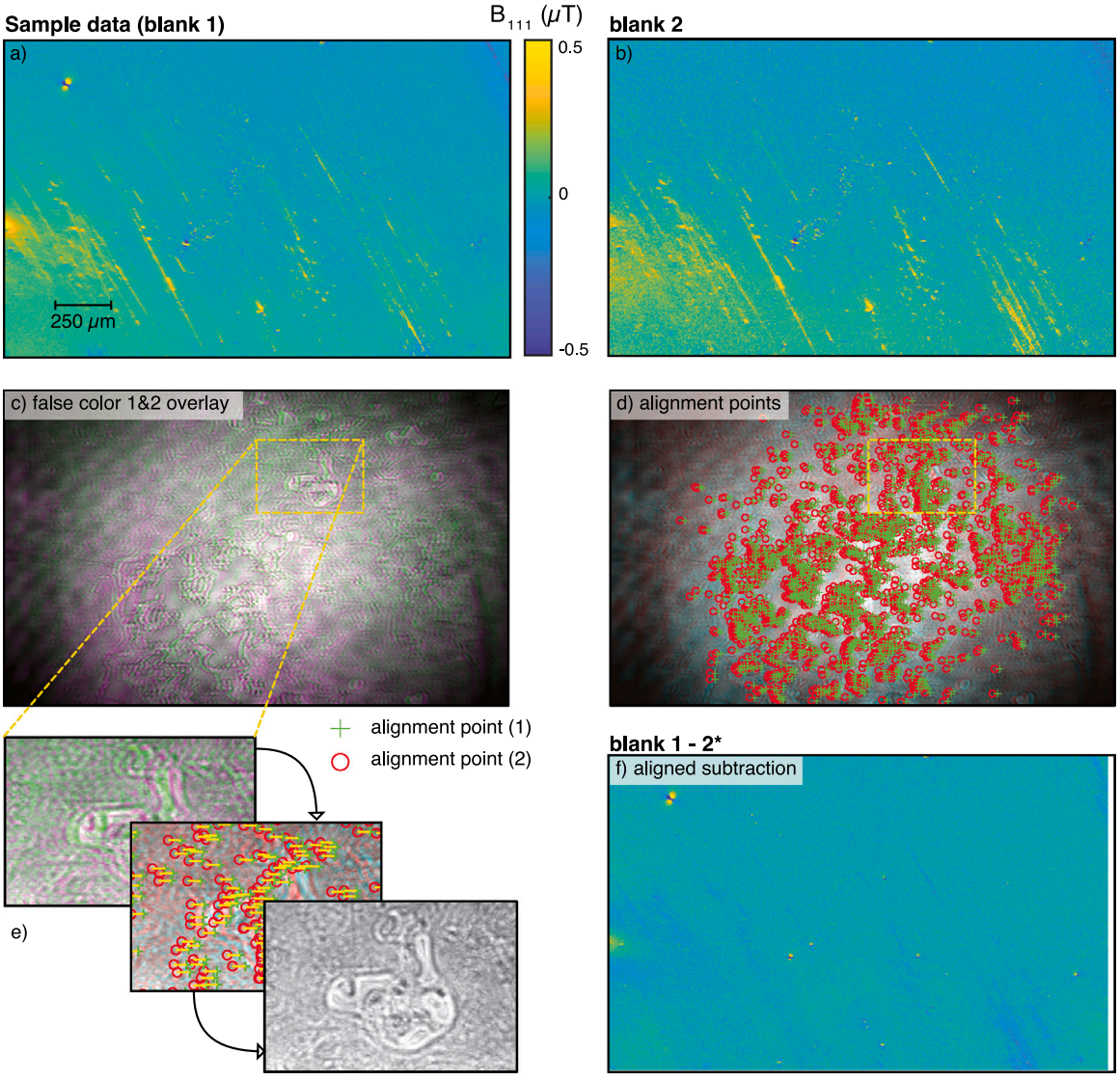

Fig. 5. Blank subtraction (`subtract_blank`) demonstrated on a blank map. Maps a, b, and f have the same color-scale. (a) Blank map to be corrected. Dipole like signal in the left top corner is cause by small dust particle on the diamond with a moment of $\approx 3 \times 10^{-14} Am^2$ (b) Blank to be subtracted from (a). (c) Fluorescence intensity maps for (a) and (b) overlaid in false colors showing misalignment of the diamond in the two images. (d) Alignment points detected for (a) (cross) and (b) (circle). (e) Close-up of the re-alignment of blank measurement (b) with respect to (a). Yellow lines show translation and rotation. (f) Resulting map after subtraction. Note data on the edge are missing due to non-overlapping blank data. (For interpretation of the references to color in this figure legend, the reader is referred to the web version of this article.)

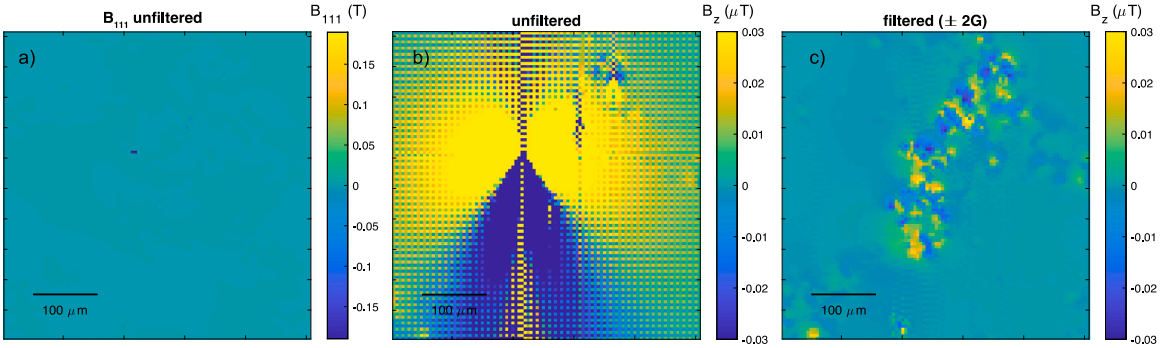

Fig. 6. Severe example of the effect of outliers on the $B_{111} \rightarrow B_z$ conversion. (a) Unfiltered B_{111} data. (b) Unfiltered B_z data, in which a single extreme pixel value due to non-physical ODMR spectrum fitting is delocalized during the conversion. (c) Data after running `threshold_QDM_map` with `threshold`,*2*.

size (step) and best-guess sensor distance (h), which are necessary for subsequent net moment analysis (Section 5.2). The final output of QDMdataprocessing is a .mat file, containing the (cropped) B_z map of either remanent or induced signal, (cropped) reflected light image, and all necessary parameters for further analysis.

5. Analysis

5.1. Qualitative map analysis

The QDM's ability to acquire reflected-light images of the exact magnetic field measurement region is especially helpful for locating ferromagnetic sources in the sample. Comparing the remanent or induced signal with the reflected light image, or plotting a superposition of both, helps to identify remanence carrying grain populations (right side Fig. 2) and to detect both dipole-like signals for further net-moment (Section 5.2) investigation and aggregates of magnetic signal for complex map analysis (Section 5.3, left side Fig. 2). The optical maps produced with the QDM magnetic field maps can also be registered to more detailed optical, electron microscope, or other maps to further investigate the source of magnetization. This type of qualitative image analysis has been used, for example, to study solar nebula magnetic fields recorded by meteorites (Fu et al., 2014, 2021c; Nichols et al., 2021), the magnetic remanence properties of single zircon crystals (Fu et al., 2017; Weiss et al., 2018; Tang et al., 2019), and the magnetic mineralogy of samples recording a strengthening paleomagnetic field during the late Ediacaran Period (Thallner et al., 2021).

5.2. Net moment analysis

Retrieving net moments from samples is a routine practice in paleomagnetism. The changes in the net magnetic moment with increasing temperature or AF field can be used to reconstruct past magnetic field directions and intensities, leading to insights about tectonic plate configurations and the geodynamo. The signal measured with traditional magnetometers, however, represent the sum over all sources in the typically centimeter-scale sample. With the QDM, it is possible to generate the same type of data (moment magnitude, inclination, declination) at the sub-millimeter scale by fitting a dipole model to the magnetic field signal from small source regions. To estimate the net moment from a source contained in a QDM map, the signal of a source needs to be sufficiently separated from the surrounding material and dipole-like in character (see Fu et al., 2020). The following section describes QDM*lab* functions tailored towards isolating the magnetic signal of a dipole within a map and generating a best-fit magnetic moment from the data.

5.2.1. Source subtraction

QDM maps can be complex, with multiple sources clustering in a small region. The best-fit dipole to a source is only physically meaningful when it is clear that the fitted signal is dominated by a well-defined volume of ferromagnetic grains. If sources in the surrounding area contributes significantly to the fitted magnetic field, the resulting magnetization does not in general quantify the net moment of either source or of their sum. Therefore, reducing the magnetic field signal contributed by adjacent sources outside of the region of interest is key for obtaining meaningful net moment inversions.

To easily 'clean' the B_z map from extraneous sources, subtract_source creates a figure in which the user selects the top left and bottom right corners of a box containing the magnetic field signal to be removed. Using fit_source (Section 5.2.2), subtract_source calculates the best-fit dipole and subtracts its signal from a selected region of the map (Code 3). Finally a new file (Bz_uc0-dip*.mat where * is the Nth dipole) is saved to disk for further analysis.

```
cleanedMap = fit_dipole('filePath', ...
 ⟨path to data file⟩, 'fitOrder', ⟨1*,2,3⟩);
```

Code 3: Example of subtract_source with fitOrder: *1* = dipole, *2* = dipole + quadrupole, and *3* = dipole + quadrupole + octupole. Note: The use of fitOrder: *>1* can lead to non-unique solutions and has been deprecated but kept for compatibility.

5.2.2. Source fitting

After sufficiently eliminating the magnetic field signal from extraneous sources (if necessary), the B_z signal can be fitted with a dipole model to extract the magnetic moment magnitude, declination, inclination, source location and dipolarity parameter (Fu et al., 2020). Two functions, fit_source and fit_sources_series are available in QDM*lab*. The fitting component of both functions uses the MATLAB internal least-squares fmincon (method=1; constrained=false), and fminsearch (method=1; constrained=true), or Nelder–Mead based lsqnonlin (method=2) fitting routines. These routines have been used previously to generate net moment data from QDM maps (e.g. Fu et al., 2020).

Prior to running either fit_sources_series or fit_source the map may benefit from upward continuation (upward_continue, upCont [μm]), which computes the expected magnetic field map if measured at a different sensor-to-sample height. Changing the measurement height can dramatically increase the dipolarity of the source and yield more reliable net moments (see Fu et al., 2020).

fit_source fits a single dipole, quadrupole, or octupole (fitOrder; *1**,*2*,*3*) to a single source in a map. In fit_source, the location of the source can either be picked directly on the map or specified with xy in pixels and will be optimized together with the depth during the fitting process. The keyword cropFactor defines the edge length of a square in pixels, which restricts the fitted data region. Running the function creates a plot with the data, model and residuals (Fig. 7a,b,c) of the fitting region (marked in red) and a figure with the complete map and reflected light image (Fig. 7d,e).

Sometimes, such as when a background gradient is present in the QDM map, the nominally best-fitted source height can lie outside of the physical sample. For cases like this, the source height can be constrained (constrained=true) with minheight and maxheight.

Often the purpose of demagnetization experiments is to study the changes in net moment of multiple sources with increasing temperature or alternating field (AF). If done manually, fitting each source in each maps can be a tedious and error-prone task. fit_sources_series allows the user to fit multiple sources in a series of maps (e.g. of an AF-demagnetization sequence) automatically at the expense of some control of the individual fitting parameters (e.g., fitOrder). Calling fit_sources_series opens a reference map (determined by refIdx=1*) where the user can visually mark the fitting region. To ensure consistent results the maps are first aligned with respect to the reference (refIdx) (similar to subtract_blank). Finally all sources in each map are fitted and a structure of size i×j×k (i sources, j maps, k upward continuation distances) with the results is returned and saved to a plain text file (save).

```
results = fit_source(
    'filePath', ⟨path to data file⟩, ...
    'fitOrder', ⟨1*,2,3⟩, ...
    'xy', ⟨[int, int]⟩, ...
    'cropFactor', ⟨int⟩, ...
    'upCont', ⟨in μm⟩, ...
    'constrained', ⟨true, false*⟩, ...
    'minheight', ⟨in m⟩, ...
    'maxheight', ⟨in m⟩)
```

Code 4: Example of the fit_source function parameters and options. (see. Fig. 7). Note: The use of fitOrder: *>1* can lead to non-unique solutions and has been deprecated but kept for compatibility.

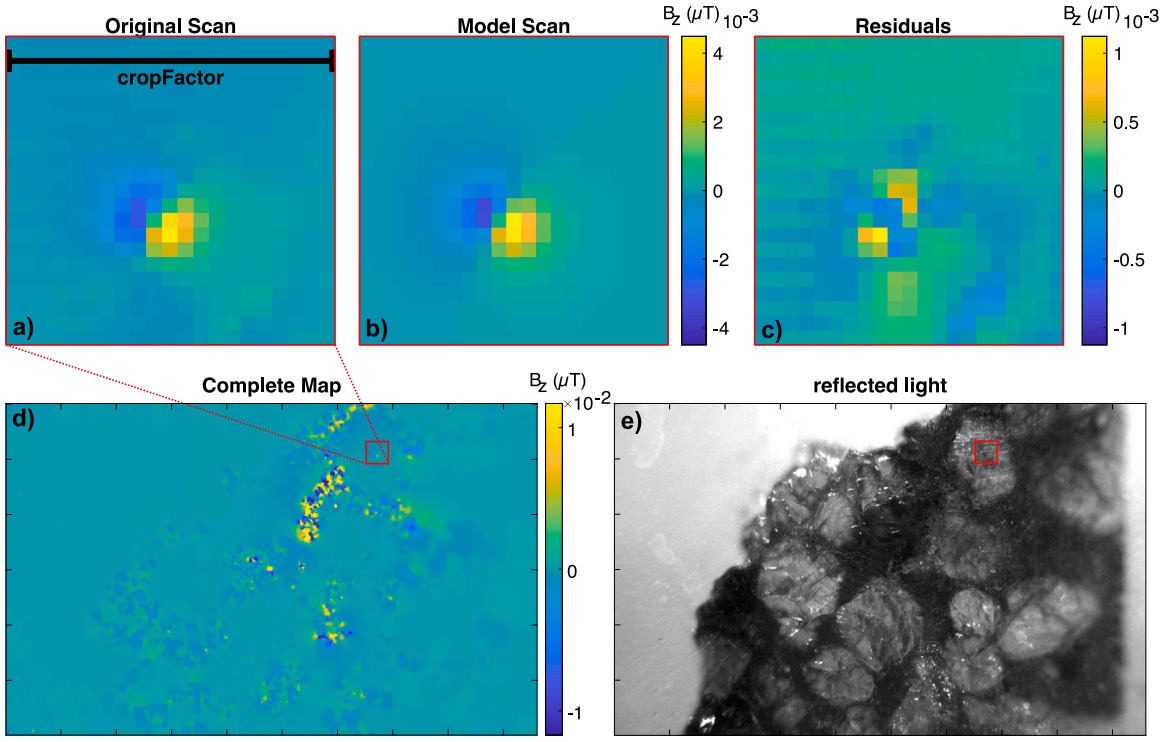

Fig. 7. Source fitting in QDM*lab* with `fit_source`. (a) Data, (b) the fitted model, and (c) the residuals of the source region. The size of the region can be changed with `cropFactor`. The source region shown in a–c and in the corresponding reflected light image (e) is marked with a red square in the full map (d).

5.3. Complex map analysis

While net moment analysis provides the most quantitative description of magnetization, often, magnetic maps show a more complex behavior (i.e. not simple dipoles), making it impossible to obtain accurate information using methods described in Section 5.2. By complex we do not refer to the mathematical set of complex numbers but merely the complicated nature of the field structure within magnetic maps. Still, important information regarding the unblocking behavior of ferromagnetic grains can be extracted from such maps. The following section describes functions (Fig. 2b left), which can be used to determine information on the demagnetization behavior and general magnetic properties of parts of more complicated magnetic field sources that are not amenable to net moment analysis.

5.3.1. Demagnetization behavior

In paleo- and rock-magnetism, a crucial piece of information is the AF or thermal unblocking spectrum of the magnetic remanence carriers (e.g. Dunlop and Özdemir, 1997). For instance, the coercivity and thermal unblocking of a sample are indicative of the magnetic domain state and the ability to retain a natural remanent magnetization (NRM) over geologic time (Pullaiah et al., 1975).

While QDM images can correlate magnetic signals with observed magnetic grain populations, it is often ambiguous whether a given set of magnetic grains carry the NRM component of interest. Distinguishing the demagnetization behaviors of different grain-populations within a sample can be used to robustly correlate NRM components identified in bulk sample analysis with their magnetic carrier population (Volk et al., 2021; Brenner et al., 2021).

A more sophisticated, robust, and broadly applicable version of the analysis used in Volk et al. (2021) is implemented in QDM*lab* (`demag_behavior`). Similar to the blank measurement subtraction, all maps (e.g., from an AF or thermal demagnetization sequence) need to be aligned with respect to a reference map. `demag_behavior` automatically detects features in the reflected light images (see `subtract_blank`), calculates the translation and rotation between all maps, and transforms the magnetic data accordingly (Fig. 8a–f). A map of the NRM as a reference is a typical choice for coercivity or thermal unblocking analysis. Other remanence types, for example an isothermal remanent magnetization for backfield coercivity determination, can also be used. By default, the first map in the `cell` of folders (`nFolders`) is the reference map (`fixedIdx`=1).

In the reference map (Fig. 8a), the user manually selects regions of interest (ROI). As an example, the ROI may contain a single magnetite crystal, a cluster of particles, or a layer of magnetic material. Within that ROI `demag_behavior` creates a selection containing all pixels with field values exceeding a percentage (`selectionThreshold`=`0.25`*) of the maximum field. This selection is applied to all previously aligned maps, and the number of pixels with positive field values are counted. In other words, `demag_behavior` detects polarity reversals in the strongest pixels of the ROI. Unlike bulk sample techniques, the QDM measures magnetizations at a grain scale. Instead of gradually demagnetizing, the magnetization of a small grain flips polarity instantaneously when the AF field strength surpasses the coercivity of the grain. Thus, changes in field polarity within an area are a better way to detect the demagnetization behavior than other methods (e.g., mean magnetic field). Furthermore, simple counting of polarity changes proved more robust against small differences in the sample-sensor height among measurements, for example.

Some additional options can be passed to `demag_behavior` to make the calculation more robust. Small changes in the sample-diamond distance can be corrected with `upCont` by passing a `cell` with the desired upward continuation (`upward_continue`) for each map according to their index in `nFolders`.

Since `x`/`y` transformation is only accurate to within a few pixels, `demag_behavior` has the option to estimate the errors stemming from misalignment using a bootstrap approach. Passing `bootStrapN` (number of iterations) $\langle >0 \rangle$, each map is shifted by a number of pixels (`pixelShift`) picked from a uniform distribution of pseudorandom integers along ±`x`, and ±`y`. For each iteration, the number of positive pixels is calculated. `demag_behavior` returns the mean and one σ error.

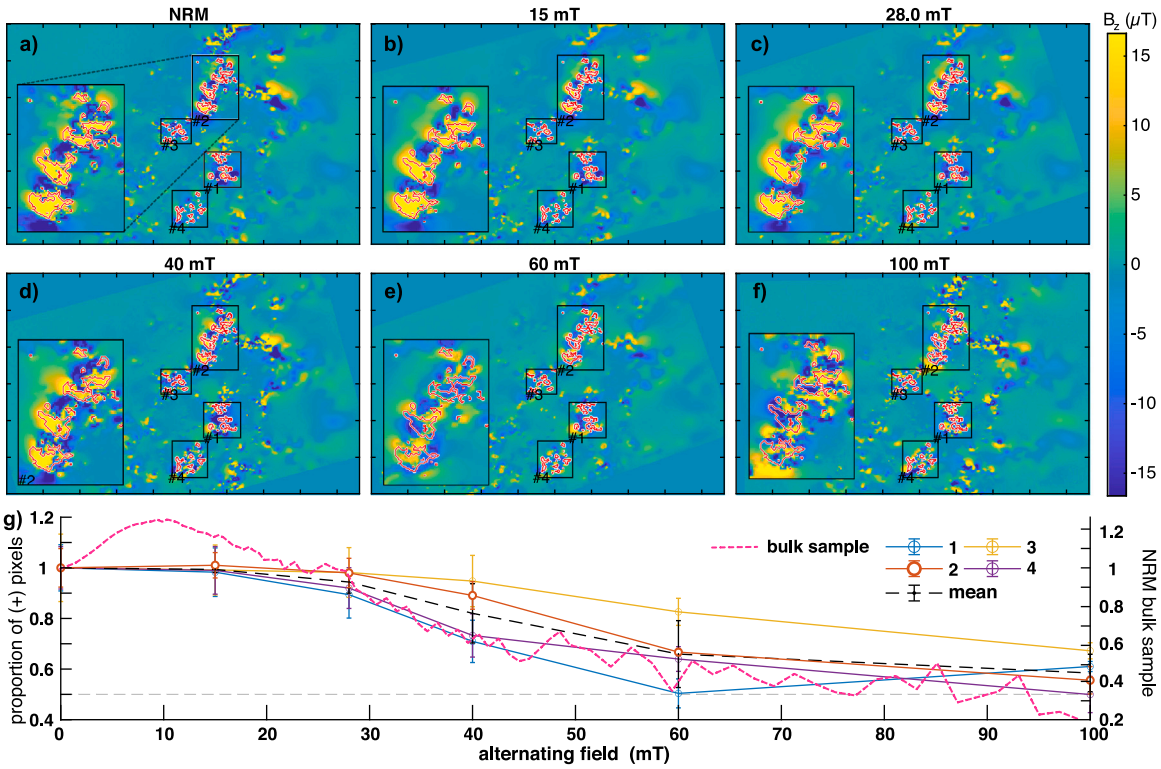

Fig. 8. Estimation of the demagnetization behavior of Ti-magnetite crystals in the martian meteorite MIL 03346 with `demag_behavior`. (a–f) show maps aligned with respect to the NRM map at different stages of an AF demagnetization sequence. (g) shows the number of positive pixels counted in each ROI normalized to the NRM and the average of all 4 ROI (black dashed line). Error-bars are 1σ error for 1000 calculations each with a random mean shift of the selection by ± 3 pixels in x and y direction. Code example used to calculate the data can be seen in Code 5. Pink line shows the bulk NRM AF-demagnetization of the same sample slice measured with a SQUID rock magnetometer. Note that convergence to 0.5 for the proportion of positive pixels in the QDM map signifies full demagnetization. (For interpretation of the references to color in this figure legend, the reader is referred to the web version of this article.)

```
nFolders = ⟨cell with 6 folders⟩;
filterProps = struct('threshold', 2);
results = demag_behavior(nFolders, ...
  'fixedIdx', ⟨1*⟩
  'bootStrapN', 1000, 'pixelShift', 3, ...
  'upCont', ⟨cell with 6 × upward cont. in μm⟩, ...
  'filterProps', filterProps);
```

Code 5: Example code for determining the demagnetization behavior from QDM images using `demag_behavior`. Results can be seen in Fig. 8.

The example in Fig. 8 shows the demagnetization behavior of individual exsolved Ti-magnetite assemblages (Code 5). For up to 40 mT, the field patterns do not change significantly. With increasing AF-field, the number of positive pixels approaches 0.5, which is the theoretical threshold for a demagnetized grain. The example in Fig. 8 shows that the AF demagnetization of the NRM of the meteorite (MIL 03346) measured with a SQUID magnetometer, gives compatible results as those from `demag_behavior`.

5.3.2. Viscous magnetization

Viscous magnetization (VM) describes the change of the magnetization direction and intensity over time in the presence of a magnetic field (e.g. Yu and Tauxe, 2006). VM can be measured on rock magnetic equipment like the vibrating and alternating gradient sample magnetometers (e.g. Foner and McNiff Jr., 1968) or other special paleomagnetic instruments (Le Goff and Gallet, 2004). Due to limitations in sensitivity of these instruments only measurements on bulk magnetic materials were possible, until now. The significantly higher sensitivity of the QDM, together with its spatial resolution, makes it the ideal tool to visualize and distinguish between viscous and non-viscous populations of magnetization carriers.

QDM magnetic field maps are typically measured in an applied magnetic field (see Section 1, Glenn et al. (2017)), which can introduce VM components. The default measurement protocol contains four separate measurement sweeps. The field polarity is switched after the first and third measurement, resulting in a protocol (B↑ B↓B↓ B↑) that minimizes the net VM signal. Graphically, the area under the curve in Fig. 9a), which denotes the integrated VM signal, sums to nearly zero in this protocol. In contrast, a protocol with only a simple switch (B↑B↓) would result in a VM signal from viscous grains. Here, we are using this effect to map the viscosity of grain populations qualitatively.

We measure the same FOV using both protocols, generating a non-viscous (B↑ B↓B↓ B↑) Fig. 9b) and viscous Fig. 9c) (B↑B↓) map. This additional step could however be omitted by saving a raw data-set after the first B↓ interval using the QDM data acquisition software, yielding the viscosity information with no additional measurement time. The maps can be aligned and subtracted automatically with `viscosity`, revealing viscous regions in the map.

Fig. 9d shows the viscous parts of the martian meteorite ALH 84001. ALH 84001 contains two kinds of remanence-carrying minerals, carbonates with fine-grained magnetite and chromite assemblages with pyrrhotite inclusions (Weiss et al., 2002). Both can be seen in Fig. 9b and have been argued to carry a stable, ancient (3.9–4.1 Ga) record of the martian paleomagnetic field (Weiss et al., 2002). The differences in the non-viscous map in Fig. 9b and Fig. 9c are subtle. After subtraction, however, it is clear that some of the carbonates acquire a VM while the chromite grains (pink box in Fig. 9a,b,c) do not.

6. Conclusions

Magnetic imaging with the QDM allows the measurement of samples at unprecedented micrometer resolution and sensitivity (10^{-16}

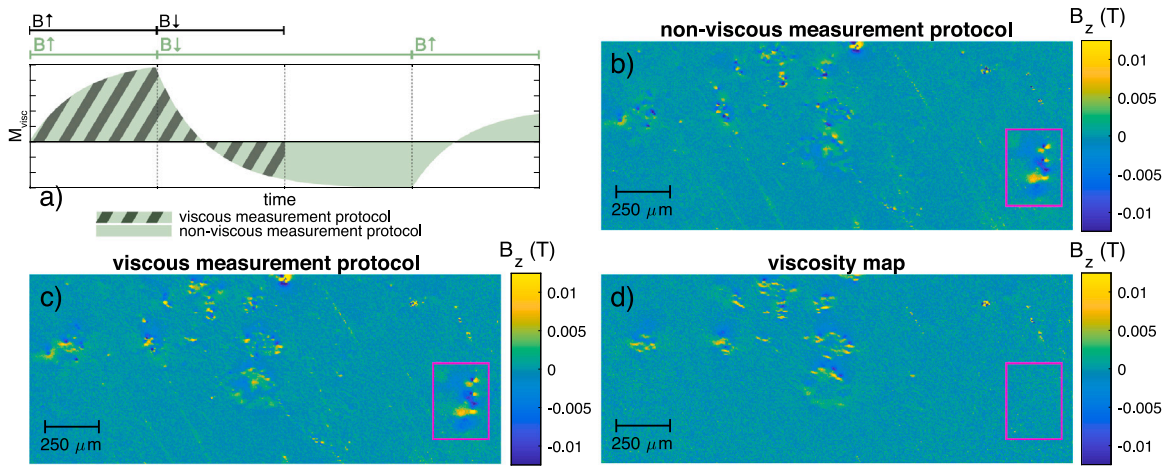

Fig. 9. (a) Illustration of the protocol for measuring *non*-viscous and *viscous* (dashed) data. a–c) Cropped QDM map of the martian meteorite ALH 84001 (Steele et al., 2019). (b) Standard (B↑ B↓B↓ B↑) *non*-viscous protocol. (c) (B↑B↓) *viscous* protocol. (d) Viscosity map (maps b-c) magnetic carrier minerals able and unable (pink box) to acquire viscous remanence. (For interpretation of the references to color in this figure legend, the reader is referred to the web version of this article.)

Am^2). However, QDM measurements consist of large amounts of data that must be reduced to generated a magnetic field map, which is followed by a range of possible analysis pathways. Prior to this work, no comprehensive software package was available for these tasks. QDM*lab* is an actively-developed, open-source, integrated MATLAB framework for calculating and analyzing QDM magnetic maps of geologic samples. With the use of GPU fitting routines, spectral algorithms, and image recognition, QDM*lab* quickly and robustly calculates and corrects B_{111} and B_z maps from raw ODMR spectra at each camera pixel.

Easy-to-use map editing features such as map filtering and cropping as well as blank and source subtraction are implemented to maximize the final map quality. Finally, analysis functions (`fit_source`, `demag_behavior`, `viscosity`) enable studies of rock and mineral samples in ways novel ways. With slight adjustments, the routines in QDM*lab* can be applied to other kinds of magnetic field maps (e.g. SQUID-microscope) and used for materials other than geologic samples (e.g. biological) thereby enabling magnetic map analysis for a broad variety of scientific disciplines.

CRediT authorship contribution statement

Michael W.R. Volk: Wrote the manuscript, Led the development of QDMlab. **Roger R. Fu:** Supervision of project, Significant contributions to code-base. **Raisa Trubko:** Contributed in equal parts to the code-base. **Pauli Kehayias:** Contributed in equal parts to the code-base. **David R. Glenn:** Contributed in equal parts to the code-base. **Eduardo A. Lima:** Contributed in equal parts to the code-base.

Declaration of competing interest

The authors declare that they have no known competing financial interests or personal relationships that could have appeared to influence the work reported in this paper.

Data availability

Data will be made available on request.

Acknowledgments

We thank participants of the Magnetic Imaging in Rock Magnetism and Paleomagnetism Workshop held at UC Berkeley in December 2019 for insightful discussions. RRF, MWRV, and RT were supported by National Science Foundation (NSF) , USA Grants PHY-1843727 and EAR-1847042. EAL would like to thank NSF, USA (DMS-1521765) and NASA, USA (NNX15AH72G) for partial support.

Code availability section The source code, and toolbox container (.mltbx) are published can be downloaded at https://github.com/HarvardPaleomag/QDMlab. A set of raw and processed data for testing is available at https://doi.org/10.7910/DVN/MPMNZI (Volk et al., 2022).

Appendix A. Supplementary data

Supplementary material related to this article can be found online at https://doi.org/10.1016/j.cageo.2022.105198.

References

Brenner, A.R., Fu, R.R., Hudak, G.J., Foley, B.J., 2021. Plate motion and a dipolar geomagnetic field at 3.25 Ga. submitted for publication.

Chang, L., Hong, H., Bai, F., Wang, S., Pei, Z., Paterson, G.A., Heslop, D., Roberts, A.P., Huang, B., Tauxe, L., Muxworthy, A.R., 2020. Detrital remanent magnetization of single-crystal silicates with magnetic inclusions: constraints from deposition experiments. Geophys. J. Int. 224 (3), 2001–2015.

Dunlop, D.J., Özdemir, O., 1997. Rock Magnetism. Cambridge University Press, Cambridge, Series Title.

Dunlop, D.J., West, G.F., 1969. An experimental evaluation of single domain theories. Rev. Geophys. 7 (4), 709.

Fischer, R., Jarmola, A., Kehayias, P., Budker, D., 2013. Optical polarization of nuclear ensembles in diamond. Phys. Rev. B 7, 00096.

Foner, S., McNiff Jr., E.J., 1968. Very low frequency integrating vibrating sample magnetometer (VLFVSM) with high differential sensitivity in high dc fields. Rev. Sci. Instrum. 39 (2), 171–179.

Fu, R.R., Hess, K., Jaqueto, P., Novello, V.F., Kukla, T., Trindade, R.I.F., Stríkis, N.M., Cruz, F.W., Ben Dor, O., 2021a. High-resolution environmental magnetism using the quantum diamond microscope (QDM): Application to a tropical speleothem. Front. Earth Sci. 8, 604505.

Fu, R.R., Lima, E.A., Volk, M.W.R., Trubko, R., 2020. High-sensitivity moment magnetometry with the quantum diamond microscope. Geochem., Geophys., Geosyst. 21 (8), e2020GC009147, ZSCC: 0000000 _eprint: https://onlinelibrary.wiley.com/doi/pdf/10.1029/2020GC009147.

Fu, R.R., Volk, M.W.R., Bilardello, D., Libourel, G., Lesur, G., Dor, O.B., 2021b. The fine-scale magnetic history of the allende meteorite: Implications for the structure of the solar nebula. AGU Adv..

Fu, R.R., Volk, M.W.R., Bilardello, D., Libourel, G., Lesur, G.R.J., Dor, O.B., 2021c. The fine-scale magnetic history of the allende meteorite: Implications for the structure of the solar nebula. AGU Adv. 2 (e2021AV000511), 21. http://dx.doi.org/10.1029/2021AV000486, 00000.

Fu, R.R., Weiss, B.P., Lima, E.A., Harrison, R.J., Bai, X.-N., Desch, S.J., Ebel, D.S., Suavet, C., Wang, H., Glenn, D.R., Le Sage, D., Kasama, T., Walsworth, R.L., Kuan, A.T., 2014. Solar nebula magnetic fields recorded in the Semarkona meteorite. Science 346 (6213), 1089–1092.

Fu, R.R., Weiss, B.P., Lima, E.A., Kehayias, P., Araujo, J.F., Glenn, D.R., Gelb, J., Einsle, J.F., Bauer, A.M., Harrison, R.J., Ali, G.A., Walsworth, R.L., 2017. Evaluating the paleomagnetic potential of single zircon crystals using the Bishop Tuff. Earth Planet. Sci. Lett. 458, 1–13.

Glenn, D.R., Fu, R.R., Kehayias, P., Le Sage, D., Lima, E.A., Weiss, B.P., Walsworth, R.L., 2017. Micrometer-scale magnetic imaging of geological samples using a quantum diamond microscope. Geochem., Geophys., Geosyst. 18 (8), 3254–3267, arXiv:1605.08479.

Glenn, D.R., Lee, K., Park, H., Weissleder, R., Yacoby, A., Lukin, M.D., Lee, H., Walsworth, R.L., Connolly, C.B., 2015. Single-cell magnetic imaging using a quantum diamond microscope. Nature Methods 12 (8), 736–738.

Hsieh, S., Bhattacharyya, P., Zu, C., Mittiga, T., Smart, T.J., Machado, F., Kobrin, B., Höhn, T.O., Rui, N.Z., Kamrani, M., Chatterjee, S., Choi, S., Zaletel, M., Struzhkin, V.V., Moore, J.E., Levitas, V.I., Jeanloz, R., Yao, N.Y., 2019. Imaging stress and magnetism at high pressures using a nanoscale quantum sensor. Science 366 (6471), 1349–1354.

Kehayias, P., Turner, M.J., Trubko, R., Schloss, J.M., Hart, C.A., Wesson, M., Glenn, D.R., Walsworth, R.L., 2019. Imaging crystal stress in diamond using ensembles of nitrogen-vacancy centers. Phys. Rev. B 100 (17), 174103.

Le Goff, M., Gallet, Y., 2004. A new three-axis vibrating sample magnetometer for continuous high-temperature magnetization measurements: applications to paleo- and archeo-intensity determinations. Earth Planet. Sci. Lett. 229 (1–2), 31–43.

Levine, E.V., Turner, M.J., Kehayias, P., Hart, C.A., Langellier, N., Trubko, R., Glenn, D.R., Fu, R.R., Walsworth, R.L., 2019. Principles and techniques of the quantum diamond microscope. Nanophotonics 8 (11), 1945–1973. http://dx.doi.org/10.1515/nanoph-2019-0209.

Lima, E.A., Weiss, B.P., 2016. Ultra-high sensitivity moment magnetometry of geological samples using magnetic microscopy. Geochem., Geophys., Geosyst. 17 (9), 3754–3774, 00009, arXiv:1605.08479.

McClelland, E., 1996. Theory of CRM acquired by grain growth, and its implications for TRM discrimination and palaeointensity determination in igneous rocks. Geophys. J. Int. 126 (1), 271–280, ZSCC: 0000061 Publisher: Oxford Academic.

Nichols, C.I.O., Bryson, J.F.J., Cottrell, R.D., Fu, R.R., Harrison, R.J., Herrero-Albillos, J., Kronast, F., Tarduno, J.A., Weiss, B.P., 2021. A time-resolved paleomagnetic record of main group pallasites: Evidence for a large-cored, thin-mantled parent body. J. Geophys. Res.: Planets 126 (7), http://dx.doi.org/10.1029/2021JE006900, 00000.

Przybylski, A., Thiel, B., Keller-Findeisen, J., Stock, B., Bates, M., 2017. Gpufit: An open-source toolkit for GPU-accelerated curve fitting. Sci. Rep. 7 (1), 15722.

Pullaiah, G., Irving, E., Buchan, K.L., Dunlop, D.J., 1975. Magnetization changes caused by burial and uplift. Earth Planet. Sci. Lett. 28 (2), 133–143.

Steele, S., Volk, M., Fu, R.R., 2019. Investigating the early martian magnetic field using chromite in the ALH 84001 meteorite. In: AGU Fall Meeting Abstracts. pp. GP43B–0796.

Tang, F., Taylor, R.J.M., Einsle, J.F., Borlina, C.S., Fu, R.R., Weiss, B.P., Williams, H.M., Williams, W., Nagy, L., Midgley, P.A., Lima, E.A., Bell, E.A., Harrison, T.M., Alexander, E.W., Harrison, R.J., 2019. Secondary magnetite in ancient zircon precludes analysis of a Hadean geodynamo. Proc. Natl. Acad. Sci. 116 (2), 407–412, 00017.

Thallner, D., Biggin, A.J., McCausland, P.J.A., Fu, R.R., 2021. New paleointensities from the skinner cove formation, newfoundland, suggest a changing state of the geomagnetic field at the Ediacaran-Cambrian transition. J. Geophys. Res.: Solid Earth http://dx.doi.org/10.1029/2021JB022292, 00000.

Volk, M.W., Feinberg, J.M., 2019. Domain state and temperature dependence of pressure remanent magnetization in synthetic magnetite: Implications for crustal remagnetization. Geochem., Geophys., Geosyst. (May), 1–11.

Volk, M.W.R., Fu, R.R., Mittelholz, A., Day, J.M.D., 2021. Paleointensity and rock magnetism of martian nakhlite meteorite miller range 03346: Evidence for intense small-scale crustal magnetization on mars. J. Geophys. Res.: Planets 126 (5).

Volk, M., Fu, R., Raisa, T., Kehayias, P., Glenn, D.R., Lima, E.A., 2022. QDMlab example data. http://dx.doi.org/10.7910/DVN/MPMNZI.

Weiss, B.P., Fu, R.R., Einsle, J.F., Glenn, D.R., Kehayias, P., Bell, E.A., Gelb, J., Araujo, J.F., Lima, E.A., Borlina, C.S., Boehnke, P., Johnstone, D.N., Harrison, T.M., Harrison, R.J., Walsworth, R.L., 2018. Secondary magnetic inclusions in detrital zircons from the Jack Hills, Western Australia, and implications for the origin of the geodynamo. Geology 46 (5), 427–430, 00023.

Weiss, B.P., Lima, E.A., Fong, L.E., Baudenbacher, F.J., 2007. Paleointensity of the Earth's magnetic field using SQUID microscopy. Earth Planet. Sci. Lett. 264 (1–2), 61–71.

Weiss, B.P., Vali, H., Baudenbacher, F.J., Kirschvink, J.L., Stewart, S.T., Shuster, D.L., 2002. Records of an ancient Martian magnetic field in ALH84001. Earth Planet. Sci. Lett. 201 (3), 449–463, ZSCC: 0000156.

Yu, Y., Tauxe, L., 2006. Acquisition of viscous remanent magnetization. Phys. Earth Planet. Inter. 159 (1–2), 32–42.